Effective Interfacial Energy Band Engineering Strategy toward High-performance Triboelectric Nanogenerator

Xinkai Xie[1, 2, 3, #], Yuxiao Fang[2, 3, 4, #], Cheng Lu[1], Yi Tao[1], Li Yin[2, 3], Yibo Zhang[2], Zixin Wang[2], Shiyan Wang[2], Jianwen Zhao[4], Xin Tu[3], Xuhui Sun[1], Eng Gee Lim[2], Chun Zhao[2, *], Yina Liu[2, *], Zhen Wen[1, *]

[1] Institute of Functional Nano and Soft Materials (FUNSOM), Jiangsu Key Laboratory for Carbon-Based Functional Materials and Devices, Soochow University, Suzhou 215123, China.

[2] School of Advanced Technology, School of Science, Xi'an Jiaotong-Liverpool University, Suzhou 215123, China.

[3] Department of Electrical and Electronic Engineering, University of Liverpool, Liverpool L693GJ, United Kingdom.

[4] Printable Electronics Research Centre, Suzhou Institute of Nano-Tech and Nano-Bionics, Chinese Academy of Sciences, Suzhou 215123, China.

[#] X. Xie, and Y. Fang contributed equally to this work.

*Corresponding Author: Chun.Zhao@xjtlu.edu.cn (C. Zhao); Yina.Liu@xjtlu.edu.cn (Y. Liu); wenzhen2011@suda.edu.cn (Z. Wen).

Abstract

Provided that electron transition ascribed to overlapping electron dominates the mechanism of contact electrification of triboelectric nanogenerators (TENGs), the electron transfer process occurs due to the built-up electric field between the triboelectrification surface and bottom electrode. In this work, we embed a solution-processed high-permittivity electron blocking layer (HPEBL) of LaZrO into the classical contact-separation mode TENG to build an energy barrier ($\Delta E > 1.3$ eV) between ITO and PDMS, which could effectively block the transportation of electrons towards the bottom electrode. The surface potential decline rate of PDMS is obviously suppressed, extending the half-charge decay time by ~3.1 times. A $La_{0.1}Zr_{0.9}O_x$ HPEBL based TENG (H-TENG) demonstrates the electrical outputs with 215 V, 96.3 mA m^{-2} and 243.3 μC m^{-2}. Under the external load of 100 MΩ, the average gravimetric/volumetric power density and energy conversion efficiency can be calculated to be 59.34 μW g^{-1}, 152.5 μW cm^{-3} and 39.2%, respectively. Furthermore, the dielectric behaviors of LaZrO thin films are investigated by metal-insulator-metal (MIM) devices. The Poole-Frenkel (PF) emission is found to dominate the leakage mechanism of LaZrO during operation. Consequently, increasing the relative permittivity and reducing the trap density could be indicated as the optimization orientation of HPEBL.

Graphical abstract:

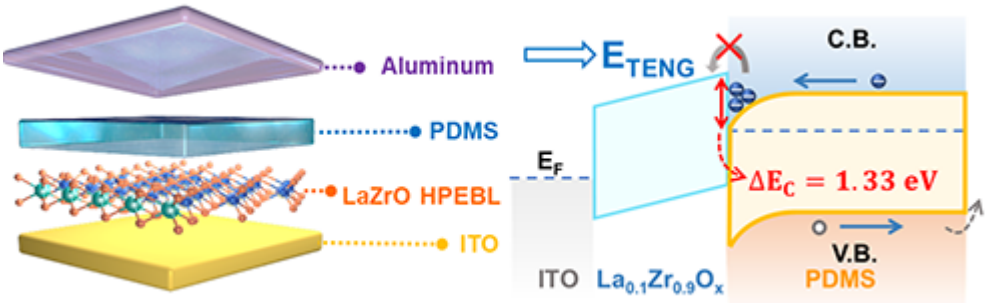

Keywords: *triboelectric nanogenerator, high-permittivity, LaZrO, energy barrier, leakage current*

1. Introduction

Originated from the second term of Maxwell's displacement current, the triboelectric nanogenerator (TENG) congregates various mechanical energy generated by the natural environment, human movement and muscle contraction, vibration energy caused by sound waves and physical equipment, fluid energy resulting from microfluid and human blood, *etc* [1-4]. Through advances in material selection and technology innovations, effective conversion of the above powers into electrical energy and implementation in self-powered sensing have been realized, including crucial applications within a wide range of industrial production, military, human-machine interaction (HMI), wireless communication and internet of healthcare things (IoHT) [5,6]. Since the surface charge density of TENG is positively correlated with the average output power and energy conversion efficiency, it plays a crucial role in determining the performance of TENG [7].

Plenty of methods have been utilized to improve the surface charge density, for instance, increasing the effective contact area, physical or chemical modification, artificial ion injection, and integrated charge excitation system [8,9]. However, according to Paschen's law, ultrahigh voltage potential difference will break down the air and result in the surface charges diffusing into the ambient [10]. Moreover, electrons migrating in the interface could recombine with positive charges on the bottom electrode, which inflict loss of surface charges [11,12]. Thus the boosted surface charge could hardly retain for a long time [13,14]. Therefore, achieving the stable, high-performance TENG and extending the storage time of surface charges has attracted broad attention [15].

Introducing various functional layers into the TENG structure provides a practical strategy to further enhance the surface charge density and prolong the surface charge

decay time of TENG [16,17]. Zhou *et al.* added the liquid lubricant of squalane between two triboelectric layers to hinder electrostatic breakdown and diminish the loss of static surface charges by increasing the breakdown field strength requirement [18]. Internal polarization and enhanced charge induction for a stable high output TENG were achieved by the high permittivity $CaCu_3Ti_4O_{12}$ particle-based composite intermediate layer [19]. Furthermore, an rGO-AgNPs hybrid membrane acting as the charge-trapping-blocking sites considerably enhanced the output power than pristine TENG [20]. Nevertheless, investigation on the dynamic surface charge decay process, the primitive theory model of the intermediate functional layer, and the working mechanism of charge generation, accumulation, induction, and transportation by the interfacial electric field require systematic and in-depth discussion.

Incorporating high-*k* dielectrics as a high-permittivity electron blocking layer (HPEBL) has attracted much attention to effectively block the induced electron from recombination and diffusion in TENG [21]. To effectively block interfacial electron diffusion to the bottom electrode of TENG, an applicable HPEBL should have properties of high relative permittivity, low defect density, large bandgap width, large conduction band offset, and strong moisture resistance. ZrO_2 and La_2O_3 have been regarded as potential candidates due to their high dielectric constants (ZrO_2~22, La_2O_3~27), large bandgap and good thermodynamic stability [22-25]. Nevertheless, ZrO_2 crystallizes at relatively low annealing temperatures (~500°C) and La_2O_3 suffers from water and carbonate absorption, both of which result in increased leakage currents and poor device properties [26-28]. By combining the Zr and La components into ternary lanthanum zirconium oxides (LaZrO), it may be possible to take advantage of the inherent properties of Zr and La while suppressing crystallization and eliminating carbonate and water absorption [29-31]. Compared to Zr, La is an ideal dopant due to

its lower standard electrode potential (SEP) (Zr=-1.45 V, La=-2.37 V), lower electronegativity (Zr=1.3, La=1.1), higher bond dissociation energy (Zr =766 kJ mol^{-1}, La=798 kJ mol^{-1}) with O, and La can effectively combine with O and reduce the oxygen vacancy (V_o) density among ZrO_2 thin films [32-34]. Consequently, modification of Zr-based oxide dielectric via a small amount of La has been proven to increase permittivity, reduce the defect states, and suppress oxygen vacancies [35]. Furthermore, the solution-processed preparation method is compatible with TENG, and the defects density (oxygen vacancies, hydroxyl groups, and dangling bonds) could be controlled by the post-treatment condition. Doping La_2O_3 into ZrO_2 could eliminate the water adsorption and improve the stability of HPEBL.

In this work, we proposed a solution-processed HPEBL based TENG (H-TENG). The outputs of $La_{0.1}Zr_{0.9}O_x$ H-TENG were remarkably boosted, exhibiting high output voltage, current density, transferred charge density and maximum energy per cycle with 215 V, 96.3 mA m^{-2}, 243.3 μC m^{-2} and 12.2 μJ, respectively. Moreover, the working mechanism revealing the electron blocking process of the LaZrO intermediate layer was illustrated explicitly by the band energy diagram theory and the Kelvin Probe Force Microscopy (KPFM) results. It was detected by an AFM tip and illustrated the surface charge decay time for half potential prolongs by ~3.1 times. Furthermore, the dielectric properties and leakage behavior of LaZrO dielectrics with different La concentrations (ZrO_x, $La_{0.1}Zr_{0.9}O_x$, and $La_{0.2}Zr_{0.8}O_x$) were in-depth investigated by fabricating metal-insulator-metal (MIM) devices, demonstrating that a low level of leakage oxygen vacancies of $La_{0.1}Zr_{0.9}O_x$ could decrease leakage path generation, and thus guaranteed the high-performance TENG. The energy barrier and high relative permittivity were put forward as two essential prerequisites for the HPEBL material. Exhaustive exploration into the electron blocking ability of the H-TENG *via* charge decay curves

observed from KPFM results and interfacial leakage current, provides the concrete theoretical foundation for stable and high-output TENG, validating scientific significance and broad application prospects in the field of micro energy harvesting, Internet of Things (IoT) technology, *etc*.

2. Material and methods

2.1. Materials

Zirconium oxynitrate hydrate ($ZrO(NO_3)_2 \cdot xH_2O$, 99.5%, Aladdin), lanthanum nitrate hexahydrate ($LaN_3O_9 \cdot 6H_2O$, 99.9%, Aladdin), PDMS purchased from Acros consisting of elastomer base and curing set (10:1, weight ration), and glass flakes coated with Indium-Tin-Oxide (ITO) film (70 nm).

2.2. Synthesis of the HPEBL film

Different HPEBL films (ZrO_x, $La_{0.1}Zr_{0.9}O_x$, and $La_{0.2}Zr_{0.8}O_x$) were prepared based on solution-processed spin coating method and low-temperature annealing technology. Firstly, the ITO-coated conductive glass was ultrasonically cleaned with acetone, ethanol, and deionized water for 15 minutes, dried with a nitrogen gun, and placed in the vacuum chamber with oxygen plasma for 30 minutes hydrophilic treatment. Secondly, weigh zirconium oxynitrate hydrate of 2.312 g, 2.08 g, 1.848 g, and lanthanum nitrate hexahydrate of 0 g, 0.432 g, 0.864 g, respectively. Thirdly, add zirconium oxynitrate hydrate powder into 5 mL deionized water, stir at 70℃ for 30 minutes, and then add corresponding lanthanum nitrate hexahydrate, stir for 12 hours to obtain a clear and transparent precursor solution of 2 mol/L (La: Zr=0:10, 1:9 and 2:8). Fourthly, install a 0.22 μm filter on the syringe port, take 0.5 mL of the precursor solution and drop it on the ITO surface. Finally, spin-coating at 4000 rpm for 30 s, pre-

anneal for 15 minutes at a temperature of 125°C, then increase the temperature by 25°C every 1 minute until 350°C and anneal at 350°C for 60 min to obtain the HPEBL layers.

2.3. Fabrication of H-TENG

A piece of aluminum foil was stuck on the acrylic substrate, performing as the top electrode and the triboelectric layer 1. The elastomer base and curing of PDMS were mixed in a Petri dish. 0.8 mL PDMS mixture was dropped on the HPEBL film, spin-coated at 6000 rpm for 30 s, and then vacuum dried at 120°C for 4 h to obtain the triboelectric layer 2. **Figure S1** illustrates the whole fabrication process of the LaZrO H-TENG.

2.4. Characterizations

A scanning electron microscope (SEM, Carl Zeiss Supra 55) was used to investigate the morphology and thickness of the LaZrO films. The X-ray diffraction patterns of LaZrO layers were measured by the X-ray diffractometer (Empyrean). The transmittance of PDMS and LaZrO coatings was observed by ultraviolet-visible spectrophotometry (UV-Vis, SHIMADZU UV-2550). The ultraviolet photoemission spectroscopy (UPS) measurement of the PDMS and LaZrO thin films was characterized by an ultraviolet photoemission spectrometer (Kratos AXIS SUPRA). The X-ray photoelectron spectroscopy (XPS) of the LaZrO thin films was measured by an X-ray photoelectron spectroscopy (ULTRA DLD). The atomic force microscope conducted the CPD analysis with scanning Kevin probe (AFM-SKP, Cypher S). For the electrical output measurement of the H-TENG, an external tapping force was applied by a commercial linear mechanical motor (Winnemotor, WMUC512075-06-X) and a programmable electrometer (Keithley model 6514) was used to test the electrical output signal. During the test, the maximum distance between two triboelectric layers was 0.4

mm, and the frequency of contact-separate was set at 2.0 Hz, and the contact area remained 2 × 2 cm^2.

3. Results and discussion

3.1. Interfacial design and electrical output of the H-TENG

The H-TENG comprises four layers, namely top electrode, triboelectric layer, interfacial HPEBL, and bottom electrode. As shown in **Fig. 1a** and **Fig. S1**, the solution-processed LaZrO film performs as the HPEBL, which is embedded between the triboelectric layer of *Polydimethylsiloxane (*PDMS*)* and the bottom ITO electrode. In addition, Al operates as the top electrode and the other triboelectric layer. **Fig. 1b** illustrates the cross-sectional view scanning electron microscope (SEM) images of the $La_{0.1}Zr_{0.9}O_x$ HPEBL inserted between PDMS and a highly doped silicon wafer. By increasing the La doping content, different thicknesses of ZrO_x, $La_{0.1}Zr_{0.9}O_x$, and $La_{0.2}Zr_{0.8}O_x$ films are depicted with 35 nm, 55 nm and 60 nm.

The transmission spectra in the visible region of 300-700 nm and evaluation of the $(ahv)^2$ versus *hv* curves indicated the bandgaps of 4.21 eV, 3.95 eV, 3.98 eV, and 4 eV for pure PDMS, ZrO_x, $La_{0.1}Zr_{0.9}O_x$, and $La_{0.2}Zr_{0.8}O_x$, respectively (**Fig. S2**). Combined with the Ultraviolet Photoelectron Spectrometer (UPS) pattern results shown in **Fig. S3** and the energy band calculation formula established in **Supplementary Note S1**, it demonstrated that the valence band (VB)/conduction band (CB) levels for pure PDMS, ZrO_x, $La_{0.1}Zr_{0.9}O_x$, and $La_{0.2}Zr_{0.8}O_x$ are -8.26/-4.05 eV, -6.89/-2.94 eV, -6.7/-2.72 eV, and -6.69/-2.69 eV. Hence, an energy barrier was built between the ITO and PDMS by introducing the LaZrO HPEBL, which could effectively block the transportation of electrons toward the bottom electrode, as shown in the energy level diagram (**Fig. 1c**). Considering the relatively large film thickness of PDMS, part of electrons could be

trapped by the defects in PDMS during the transportation. Additionally, the feature of high permittivity stimulates a higher output power. From previous work, when subjected to an external electric field, the positive and negative charges within the molecule tend to separate toward opposite directions, resulting in electric polarization, which can be expressed as [19]:

$$\vec{P} = \varepsilon_0(\varepsilon_r - 1)\vec{E} \quad (1)$$

where ε_0 is the vacuum permittivity ($8.85\times 10^{-12}\, F\, m^{-1}$), ε_r is the relative permittivity, and $\vec{E}$ is the electric field strength. It can be inferred from the formula that the electric polarization enhances in the case of high permittivity material performing as the electron blocking layer. The strong electric polarization should boost charge induction on the bottom electrode. Therefore, in addition to reducing surface charges decay, HPEBL can also noticeably increase the surface charge density. Considering that the leakage current generated on the interface of the dielectric layer could weaken its feasibility to block electrons, both the corresponding calculated relative permittivity (ε_r) values and the leakage current density (J_{leak}) at 1.5 MV/cm as a function of LaZrO MIM capacitors at various La doping concentrations were summarized in **Fig. 1d** (**Supplementary Note S2**) [36]. The calculated ε_r values for ZrO_x, $La_{0.1}Zr_{0.9}O_x$, and $La_{0.2}Zr_{0.8}O_x$ HPEBL are 19.3, 22 and 22.6, respectively. The increased relative permittivity could be ascribed to the higher ε_r value of La_2O_3 (~ 27) than ZrO_2 (~ 22). Furthermore, appropriate La incorporation (10%) effectively suppressed the leakage current. **Fig. 1e** demonstrates the electrical output performance of different TENGs. For the conventional TENG without the HPEBL, the open-circuit voltage (V_{oc}), short-circuit current (I_{sc}), and transferred charge density (σ_{tr}) are 91 V, 13.7 μA, and 92.1 μC/m^2, respectively. When embedding the LaZrO intermediate layer, with the La content increasing from 0 to 20%, the highest output is achieved by $La_{0.1}Zr_{0.9}O_x$ with V_{oc}, I_{sc}, and

Q_{sc} of 215 V, 38.5 A μA and 243.3 μC m^{-2}, respectively. A comparison to recent progresses in intermediate-layer based TENGs has been described in **Fig. S4**. We can conclude that the $La_{0.1}Zr_{0.9}O_x$ H-TENG in this work exhibits both the highest relative permittivity and transferred charge density. **Fig. S5** demonstrates the output characteristic curves of different TENGs without LaZrO, with ZrO_x, $La_{0.1}Zr_{0.9}O_x$, and $La_{0.2}Zr_{0.8}O_x$. Consequently, different from normal TENG, the embedded HPEBL could enhance polarization and induce more positive charges on the bottom electrode, due to the high permittivity of LaZrO. Furthermore, the energy barrier built between triboelectric layer and bottom electrode layer effectively blocks electron transportation to the electrode, which reduces charge recombination and prolongs the surface charge decay time. The leakage current density-electrical field measurement shows the $La_{0.1}Zr_{0.9}O_x$ has the lowest leakage current under the electrical field generated during the contact electrification, proving the best electron blocking ability. Since the intermediate layer thickness increase occurring with gradual La doping concentration, the outputs of the $La_{0.1}Zr_{0.9}O_x$ H-TENG with different intermediate layer thicknesses were compared in **Fig. 1f** and **Fig. S6**. With the increasing thickness of the $La_{0.1}Zr_{0.9}O_x$ layer from 55 nm to 165 nm, fewer positive charges could be induced, and thus the outputs of V_{oc}, I_{sc}, and σ_{tr} slightly dropped to 186 V, 28.7 μA, and 221.3 μC m^{-2}. From the theoretical discussion shown in **Supplementary Note S3**, choosing a thin intermediate layer is beneficial to improve the surface charge density. As a result, the $La_{0.1}Zr_{0.9}O_x$ based H-TENG with the intermediate layer thickness of 55 nm is selected to achieve the highest electrical output, which is consistent with the deduced results. In comparison, the $La_{0.2}Zr_{0.8}O_x$ H-TENG with intermediate layer thickness of 60 nm presented the outputs of 157.9 V, 25.32 μA and 177.2 μC/m^2. It is worth noting that the outputs of $La_{0.1}Zr_{0.9}O_x$ H-TENG with intermediate layer thickness of 165 nm were

higher than the $La_{0.2}Zr_{0.8}O_x$ H-TENG with intermediate layer thickness of 60 nm. Therefore, the La doping concentration dominates the output performance instead of the intermediate layer thickness when doping different La concentrations. As shown in **Fig. 1g**, compared with recent studies on the intermediate layer induced high-performance TENG, the transferred charge density of the $La_{0.1}Zr_{0.9}O_x$ H-TENG keeps above 240 μC m^{-2}, which belongs to the extremely high level of reported research results on intermediate layer based TENG [19-21, 37-52]. Moreover, the output energy per cycle of the $La_{0.1}Zr_{0.9}O_x$ H-TENG was determined by exploiting the *V-Q* plot at the operation frequency of 2 Hz (**Fig. 1h**). Under the external load resistance of 100 MΩ, the maximum output energy of 12.2 μJ was achieved. Thus, the average gravimetric power density, volumetric power density, and energy conversion efficiency with 59.34 μW g^{-1}, 152.5 μW cm^{-3}, and 39.2% can be obtained (**Supplementary Note S4**). Moreover, the influence of the external load resistance on the output voltage and peak output power of TENG with or without $La_{0.1}Zr_{0.9}O_x$ HPEBL is explicated in **Fig. S7**. The output voltage dramatically increases from 2 MΩ to 100 MΩ. The peak output power increases gradually to the maximum value and then decreases with the increasing of the external load resistance ranging from 1 kΩ to 1 GΩ. The matching resistance is 100 MΩ. The maximum peak output power of TENG with $La_{0.1}Zr_{0.9}O_x$ HPEBL is 32.2 μW/cm^2, which is 4.9 times larger than normal TENG. According to **Fig. S8**, the output voltage of $La_{0.1}Zr_{0.9}O_x$ HPEBL based TENG shows no virtually measurable attenuation after more than continuous 6000 contact-separation cycles, exhibiting high stability.

3.2. Working mechanism of energy band engineering

The entire structure of the H-TENG evolves from a traditional contact-separation mode TENG, and the scheme description of its working mechanism about electron blocking and enhanced polarization is illustrated in **Fig. 2a**. During the contact

electrification process, attributed to the electrophilicity differences, the top electrode of aluminum is positively charged, and the triboelectric layer of PDMS is negatively charged. Since negative charges are enriched on the PDMS surface, positive charges could be induced on the bottom ITO electrode. Consequently, a built-in electric field caused by the potential difference between the bottom electrode and the triboelectric layer will be established with the direction of vertically upward. The embedded HPEBL could prohibit negative charges transferring from PDMS to ITO, and thus negative charges appear in the triboelectric layer, reducing recombination with positive charges on the electrode, which is shown in the scheme in Fig. 2a(i). As shown in Fig. 2a(ii), positive and negative charges within the molecule tend to separate toward opposite directions due to enhanced polarization caused by the high permittivity property of embedded HPEBL, and thus more induced positive charges are generated on the bottom electrode, boosting the electrical output. There are possibly two assumptions that partial surface electrons on PDMS could disappear. One is that the electric field promotes the diffusion of surface electrons towards the bottom electrode and recombination with positive charges. The other is that due to the electron concentration gradient difference, the surface electrons could be dispersed into the atmosphere and absorbed by positive ions or particles. TENG encapsulation and vacuum tests are practical approaches to reducing the loss of electrons into air. In terms of electrons diffusion into the material, an interfacial electron blocking layer should be put forward. The HPEBL plays a significant role in reducing interface charge decay and increasing the total amount of induced charges. Since the electron blocking layer having high permittivity, more positive charges could be induced on the ITO electrode ascribed to polarization. As a consequence of energy barrier built between triboelectric layer and ITO electrode, surface charge transfer from triboelectric layer to bottom electrode could be blocked by

the HPEBL, resulting in enhancing the output and extending surface charge retaining time.

According to the Gauss theorem, the *V-Q-x* relationship for TENG without the HPEBL should be expressed as [20]:

$$V = E_{air}x + E_{PDMS}d_{PDMS} = \frac{\sigma x(t)}{\varepsilon_0} - \frac{Q}{S\varepsilon_0}\left(\frac{d_{PDMS}}{\varepsilon_{r_{PDMS}}} + x(t)\right) \quad (2)$$

where Q is the amount of transferred charge, S is the contact area, ε_0 is the vacuum permittivity, and σ represents the triboelectric charge density. The thickness and permittivity of the PDMS layer are signified by d_{PDMS} and $\varepsilon_{r_{PDMS}}$, respectively. Furthermore, $x(t)$ means the distance between two triboelectric layers over time. After embedding the interfacial HPEBL, the modified formula should be:

$$V = \frac{\sigma' x(t)}{\varepsilon_0} - \frac{Q'}{S\varepsilon_0}\left(\frac{d_{PDMS}}{\varepsilon_{r_{PDMS}}} + \frac{d_{HPEBL}}{\varepsilon_{r_{HPEBL}}} + x(t)\right) \quad (3)$$

where the thickness and permittivity of the HPEBL layer are signified by d_{HPEBL} and $\varepsilon_{r_{HPEBL}}$. As seen from the deduced formula, the introduction of the HPEBL affects the output voltage. The finite element simulation by COMSOL Multiphysics compares the triboelectric potential difference of the TENGs with or without the HPEBL, as shown in **Fig. 2b**. Compared with the pristine TENG, the potential difference between Al and PDMS layer for the TENG with the HPEBL significantly increases by 2.3 times, which is consistent with the experimental measurement result. The KPFM method was utilized to further investigate the surface charge decay process to detect the contact potential difference (CPD) between Ti/Pt coated silicon tip and the PDMS layer. **Fig. 2c** illustrates that the surface potentials of PDMS for TENG without and with HPEBL are 21 mV and 311 mV, respectively. After slight contact electrification (CE) with Al for 20 times, the surface potentials of PDMS for TENG without and with HPEBL change to -102.5 mV and -954.5 mV, respectively. Hence, the ΔCPD of H-TENG is

~10.2 times larger than the pristine TENG, as shown in **Fig. 2d**. The high dielectric constant could enhance polarization and thus boost induced charges, while the EBL could block negative charges transferring from triboelectric layer towards bottom electrode via an energy barrier, extending the surface charge decay time.

The working mechanism of the $La_{0.1}Zr_{0.9}O_x$ HPEBL extending surface charge decay time is illustrated with the energy band diagram shown in **Fig. 2f-i**. When Al is separated from the PDMS, the generated electrons at the surface of PDMS are transported towards the ITO under the internal induced electrical field. Without an electron blocking layer, the electrons quickly move in the conduction band of the PDMS and escape from the ITO electrode in a short time. As a result, the surface potential of PDMS declines rapidly in a short time ($t_{1/2} \approx 122$ s), as demonstrated in **Fig. 2e**. The insets illustrate that the root-mean-square (RMS) surface roughness values of PDMS without and with the HPEBL are 2.38 nm and 2.40 nm, which barely changed after adding the intermediate layer. On the other hand, when embedding the $La_{0.1}Zr_{0.9}O_x$ HPEBL, an energy barrier ($\Delta E \approx 1.33$ eV) is built between the ITO and PDMS, which could effectively block the transportation of electrons towards ITO. The decline of the surface potential of PDMS is suppressed accordingly with $t_{1/2} \approx 383$ s. Therefore, the surface charge decay rate is significantly reduced by three times when introducing the HPEBL. The formation of the conduction and valence band edges at the interfaces during a contact-separation cycle was demonstrated in **Fig. S9** *via* the $La_{0.1}Zr_{0.9}O_x$ H-TENG. One cycle contains four steps. At step (i), Al electrode contacts with the PDMS film, accompanied with positive and negative charges generated due to contact electrification. The Fermi level (E_F) difference between the materials bend of the energy band at the interface. At step (ii), Al electrode separates from the PDMS films. Electrons are driven from ITO to Al electrode from the connection line due to the

potential difference between the two electrodes and generate a current. Meanwhile, the internal electrical field formed among the TENG leads to the electrons accumulated at the $La_{0.1}Zr_{0.9}O_x$/PDMS interface. The electrons are blocked in PDMS, resulting in higher surface potential and longer surface charge decay time compared to TENG without a blocking layer. The blocking behavior is ascribed to the high-quality $La_{0.1}Zr_{0.9}O_x$ thin film with low trap density and the large band offset (1.33 eV) between $La_{0.1}Zr_{0.9}O_x$ and PDMS. At step (iii), as the Al electrode reaches the highest point, all generated positive charges are screened, and no electrons flow between two electrodes. Notably, the electrons generated among PDMS could be diffused into the ambient and reduce the surface potential. At step (iv), Al electrode moves close to PDMS thin film. The electrons flow back from Al to ITO electrode due to the potential difference and form a current with a direction opposite to that generated in step (ii). The four steps of a contact separation cycle result in the alternative current (AC) signal output of a TENG in the external circuits. Consequently, the energy band diagram distribution becomes an important criterion for selecting EBL materials, and effective surface charge regulation could be realized, for example, extending the charge retaining time. Similar energy barriers ($\Delta E \approx 1.11$ eV and $\Delta E \approx 1.36$ eV) between ITO and PDMS were observed when embedding intermediate layers of ZrO_x and $La_{0.2}Zr_{0.8}O_x$, as demonstrated in **Fig. S10** and **Fig. S11**. Furthermore, the contact potential difference and surface charge decay pattern of ZrO_x H-TENG and $La_{0.2}Zr_{0.8}O_x$ H-TENG has been illustrated in **Fig. S12**, depicting that the half-charge decay time extended to $t_{1/2} \approx 211$ s and $t_{1/2} \approx 140$ s, respectively.

3.3. Characterizations of interfacial LaZrO HPEBL with different La doping concentrations

X-ray photoelectron spectroscopy (XPS) characterization was carried out to study the effect of La-doping on chemical bonding states of LaZrO thin films. All peaks were calibrated by C 1s (284.6 eV). To further explore the interfacial LaZrO HPEBL, the thin film composition variation induced by different La doping concentrations was investigated by deconvoluting the O 1s peaks of ZrO_x, $La_{0.1}Zr_{0.9}O_x$, and $La_{0.2}Zr_{0.8}O_x$, as shown in **Fig. 3a-c**. All spectra deconvolution was performed by Shirley's background subtraction using a Voigt function convoluting Gaussian and Lorentzian processes. O 1s peaks were divided into three peaks centered 529.5 (O_I), 531.1(O_{II}), and 532.1 eV (O_{III}). The O_I peak centered at low binding energy represents metal oxide (M-O), which are O^{2-} ions combined with Zr and La ions. The O_{II} peak centered at medium binding energy is assigned to O^{2-} ions in the oxygen-deficient regions such as oxygen vacancy (V_o). At the same time, the O_{III} peak with high binding energy is related to loosely bound oxygen such as absorbed O_2 or H_2O, -CO^3 and chemisorbed surface hydroxyl, which could be represented by metal hydroxide (M-OH).

The summarized calculated atomic percentages of M-O, V_o, and M-OH based on the area integration of O 1s peaks are displayed in **Fig. 3d**. Due to the doping of 10% La into ZrO_x thin films, the M-O percentage increases from 69.1% to 73.5%, and the V_o percentage decreases from 15.3% to 11.3%. It could be found that appropriate La doping (10%) suppressed the formation of bonded oxygen, especially the V_o, and maximized the metal-oxide (M-O) framework formation. La has higher oxygen bond dissociation energy (798 kJ mol^{-1}) with O than Zr (766 kJ mol^{-1}), and thus adding La could lower and control the total V_o concentration. However, when the La content

increased to 20%, the M-O percentage decreased from 73.5% to 66.2%, and V_o percentage increased from 11.3% to 17.7%, which was probably attributed that the annealing temperature could not provide enough energy for the complete dehydration and densification of 20% La samples.

The survey spectra showed in **Fig. 3e** demonstrate that the characteristic Zr peak intensity decreased, and the distinct La peak concentration increased with the increasing La doping concentration. The atomic ratio of La in LaZrO thin films is then calculated to be 10.82% for 10% La sample, and 23.13% for 20% La sample. CasaXPS software was used to calculated the atomic ratio at the thin films surface according to XPS survey spectra. Then the atomic ratio could be calculated through the software. As shown in **Fig. S13**, the atomic ratio of elements was calculated through equation:

$$Atomic\ ratio\ (\frac{La}{Zr}) = \frac{Peak\ area\ (La)}{Peak\ area\ (Zr)} \times \frac{Relative\ sensitivity\ factor\ (Zr)}{Relative\ sensitivity\ factor\ (La)} \quad (4)$$

The peak of La 3d and Zr 3d has the largest peak area and were selected to represent La and Zr elements, respectively. The relative sensitivity factor (RSF) of an element is a consistent for a selected element. For La and Zr, the RSF value is 47.62 and 7.04, respectively. The CasaXPS software has built-in database of RSF, and the atomic ratio is calculated by the software automatically after determining the peaks of elements.[21]

To further prove the above statement, the thermal behavior of the precursor powder was investigated by thermogravimetric analysis-differential scanning calorimetry (TGA-DSC). The precursor solution was dried at 100°C for one hour and heated from 200 to 500°C with a 10°C /min heating rate. At the annealing temperature

of 350°C shown in **Fig. 3f**, the ZrO_x, $La_{0.1}Zr_{0.9}O_x$, and $La_{0.2}Zr_{0.8}O_x$ precursors have 51.9%, 53.6%, and 59.3% weight left, respectively. In this case, the precursor weight loss of ZrO_x and $La_{0.1}Zr_{0.9}O_x$ samples are very close. In contrast, the $La_{0.2}Zr_{0.8}O_x$ precursor has more residual at this annealing temperature, corresponding to the decreased M-O and increased V_o percentage of $La_{0.2}Zr_{0.8}O_x$ thin films. Therefore, the annealing temperature is set at 350°C. Furthermore, as shown in the inset, the X-ray diffraction (XRD) patterns illustrated that amorphous LaZrO dielectric layers were successfully prepared at an annealing temperature of 350°C. As the crystallinity decreases, grain boundaries decrease, thus declining the leakage current and presenting superior insulating properties.

3.4. MIM devices for leakage current investigation

For in-depth investigation on the dielectric properties and leakage behavior of LaZrO dielectrics with different La concentrations, MIM capacitors with the structure of Al/LaZrO/ITO were prepared, as demonstrated in **Fig. 4a**, and the inset shows the optical photograph of the MIM device. The electrochemical impedance spectroscopy (EIS) measurements were carried out and the ZSimpWin software was utilized for simulation, as shown in **Fig. S14**. It demonstrates that $La_{0.1}Zr_{0.9}O_x$ thin-films display the lowest dielectric loss resistance, corresponding to its lowest film defect density and leakage current. Moreover, only the inductance and resistance of connection lines could be measured for ITO film, indicating that ITO is a conductor with low defect density (crystal imperfection and oxygen vacancies). **Fig. 4b** displays the areal capacitance-frequency (C_i-f) characteristics of at least five devices for each La concentration. The $La_{0.1}Zr_{0.9}O_x$ thin films exhibit the weakest frequency capacitance dispersion in all frequency regions, indicating the gradual decomposition of defect traps in $La_{0.1}Zr_{0.9}O_x$ thin films and the formation of the dense metal-oxide framework.

The leakage current density-electric field (J_{leak}-E) of LaZrO MIM capacitors was investigated in **Fig. 4c**. The calculated electrical field generated on ZrO_x, $La_{0.1}Zr_{0.9}O_x$, and $La_{0.2}Zr_{0.8}O_x$ thin films during TENG operation was around 0.0142 MV/cm, 0.0125 MV/cm, and 0.0122 MV/cm, respectively (**Supplementary Note S5**). According to the leakage current shown in Figure 4c and its inset, $La_{0.1}Zr_{0.9}O_x$ demonstrated the lowest leakage current, indicating the optimal electron block behavior.

The leakage mechanism should be determined to explain the reduced leakage current of $La_{0.1}Zr_{0.9}O_x$ thin films. Previous research suggested that Poole-Frenkel (PF) emission and Schottky emission are the two primary leakage current forms due to the asymmetry of forward and reverse current and temperature dependence of leakage current [53]. For standard PF emission ln(J/E) versus $E^{1/2}$ should be linear, and for standard Schottky emission, $\ln(J/T^2)$ versus $E^{1/2}$ should be linear. **Fig. 4d** and **Fig. S15** investigated the PF and Schottky emissions, respectively. As shown in **Fig. 4d**, when $E^{1/2} < 0.55$ $MV^{1/2}/cm^{1/2}$, PF emission is responsible for the leakage current; it describes how the thermal excitation of electrons may overcome the trap barrier and emit them into the dielectric conduction band, which can be expressed as the following equation:

$$J = \sigma_0 E \, exp\left[-\frac{q}{kT}\left(\Phi_t - \sqrt{\frac{qE_m}{\pi\varepsilon_0\varepsilon_{op}}}\right)\right] \quad (5)$$

where σ_0 is the conductivity without external fields, Φ_t is the trap energy barrier, and ε_{op} is the dynamic high-frequency dielectric constant. $La_{0.1}Zr_{0.9}O_x$ has the lowest V_o density, explaining the lowest leakage current and the best electron blocking ability under the electrical field (0.0142 MV/cm) generated during the contact electrification.

Fig. 4e demonstrates the mechanism of the leakage path generation; with an applied electrical field, the oxygen vacancies could transit neutral V_o to V_o^+ or V_o^{2+} through reaction (6) and (7), respectively:

$$V_o \rightarrow V_o^+ + e^- \quad (6)$$

$$V_o \rightarrow V_o^{2+} + 2e^- \quad (7)$$

where V_o is a non-conducting deep state, and the exciting V_o^{2+} state donates two delocalized free electrons. The electrons could transport during the transition of V_o and form leakage paths among the thin film, which lead to the undesired leakage current. The incorporation of La changed the size and shape of the oxygen ion migration channel in the substitution process, which was beneficial in reducing the V_o density and improving the electronic transmission. In this case, the leakage paths were reduced, and the leakage current was suppressed accordingly. The increased leakage current of 20% La sample could probably be ascribed to the incomplete dehydration of residual metal hydroxide caused by high La concentration. It is worth noting that the low breakdown electric field of ZrO_x thin film is related to the small band offset between ZrO_x and Al electrode. As shown in Figure S9, the Schottky emission is the leakage mechanism under the large electrical field ($E^{1/2} > 0.6$ $MV^{1/2}/cm^{1/2}$). Based on the electrical performances of the $La_{0.1}Zr_{0.9}O_x$ thin films, such a low level of leakage current guarantees the achievement of high-performance TENG through effective electron blocking. For practical applications, as shown in **Fig. S14**, the $La_{0.1}Zr_{0.9}O_x$ based H-TENG charged the commercial capacitor of 22 μF to ~5 V within 200 s at the frequency of 2 Hz. Furthermore, the external stimuli induced triboelectric potentials through the

$La_{0.1}Zr_{0.9}O_x$ based H-TENG, and thus activated the biological synaptic behavior, such as the excitatory postsynaptic current (EPSC) of the artificial synaptic device (e.g., AlO_x synaptic transistor), exhibiting broad application prospects in self-powered biomimetic sensors and neuromorphic network systems.

4. Conclusion

In summary, a solution-processed high-permittivity electron blocking layer (HPEBL) of LaZrO based TENG was proposed. The LaZrO intermediate layer plays a significant role in reducing interface charge decay and increasing the total amount of induced charges. Among different H-TENG of La doping concentrations varying from 0 to 20%, the device embedded with $La_{0.1}Zr_{0.9}O_x$ depicted the highest output charge density of 243.3 $\mu C/m^2$. The experimental measurement results are consistent with the outcome of the potential simulation results. KPFM images representing the dynamic potential distribution before and after contact electrification of TENGs with and without the $La_{0.1}Zr_{0.9}O_x$ HPEBL were recorded, demonstrating a dramatic increase of ΔCPD and a notable decrease of charge decay rate for the $La_{0.1}Zr_{0.9}O_x$ H-TENG. Energy band diagrams were described and illustrated that the transportation of electrons towards the bottom electrode could be effectively blocked due to the built energy barrier when embedding the HPEBL. Moreover, MIM devices based on ZrO_x, $La_{0.1}Zr_{0.9}O_x$, and $La_{0.2}Zr_{0.8}O_x$ were fabricated to elaborately analyze their dielectric properties and leakage current behaviors. As a result, suppressed V_o in $La_{0.1}Zr_{0.9}O_x$ thin film decreases the leakage current, while increased V_o in $La_{0.2}Zr_{0.8}O_x$ could generate more leakage paths and thus lead to increased leakage current under low electrical field ($E^{1/2} < 0.55$ $MV^{1/2}/cm^{1/2}$). The energy barrier built between triboelectric layer and electrode layer presents as the key factor of the electron blocking, and in-depth investigation on

influence of interfacial electric field induced leakage current illustrates the electron blocking ability. It optimizes the charge regulation mechanism and offers a general pathway to build stable and high-performance TENG, which is conducive to future applications in advanced manufacturing and intelligent self-powered sensing, such as power supply for wearable electronics, self-powered neuromorphic sensor, etc.

Declaration of Competing Interest

The authors declare that they have no known competing financial interests or personal relationships that could have appeared to influence the work reported in this paper

Acknowledgements

X. Xie and Y. Fang contributed equally to this work. This work was supported by the National Science and Technology Major Project from Minister of Science and Technology of China (No. 2021YFB3200301), the National Natural Science Foundation of China (No. 62174115), the Natural Science Foundation of the Jiangsu Higher Education Institutions of China Program (No. 19KJB510059), the Suzhou Science and Technology Development Planning Project: Key Industrial Technology Innovation (No. SYG202009, No. SYG201924), China Postdoctoral Science Foundation (No. 2021T140494), Jiangsu Key Laboratory for Carbon-based Functional Materials & Devices, Soochow University (No. KJS2157), University Research Development Fund (No. RDF-17-01-13), and the Key Program Special Fund in XJTLU (No. KSF-T-03, No. KSF-A-07). This work was partially supported by the Collaborative Innovation Center of Suzhou Nano Science & Technology, the 111 Project, Joint International Research Laboratory of Carbon-Based Functional Materials

and Devices, the XJTLU AI University Research Centre and Jiangsu (Provincial) Data Science and Cognitive Computational Engineering Research Centre at XJTLU.

Supplementary materials

The online version contains supplementary material available at xxx.

References

[1] Z. L. Wang, On Maxwell's displacement current for energy and sensors: the origin of nanogenerators, Mater. Today 20(2017) 74-82, https://doi.org/10.1016/j.mattod.2016.12.001.

[2] C. Wu, A. C. Wang, W. Ding, H. Guo, Z. L. Wang, Triboelectric Nanogenerator: A Foundation of the Energy for the New Era, Adv. Energy Mater. 9(2018) 1802906, https://doi.org/10.1002/aenm.201802906.

[3] Z. L. Wang, On the first principle theory of nanogenerators from Maxwell's equations, Nano Energy 68(2020) 104272, https://doi.org/10.1016/j.nanoen.2019.104272.

[4] Z. L. Wang, A. C. Wang, On the origin of contact-electrification, Mater. Today 30(2019) 34-51, https://doi.org/10.1016/j.mattod.2019.05.016.

[5] Q. Shi, B. Dong, T. He, Z. Sun, J. Zhu, Z. Zhang, C. Lee, Progress in wearable electronics/photonics-Moving toward the era of artificial intelligence and internet of things, Infomat 2(2020) 1131-1162, https://doi.org/10.1002/inf2.12122.

[6] H. Verma, N. Chauhan, N. Chand, L. K. Awasthi, Buffer-loss estimation to address congestion in 6LoWPAN based resource-restricted 'Internet of Healthcare Things' network, Comput. Commun. 181(2022) 236-256, https://doi.org/10.1016/j.comcom.2021.10.016.

[7] C. Zhang, L. Zhou, P. Cheng, X. Yin, D. Liu, X. Li, H. Guo, Z. L. Wang, J. Wang, Surface charge density of triboelectric nanogenerators: Theoretical

552 boundary and optimization methodology, Appl. Mater. Today 18(2020) 100496,
553 https://doi.org/10.1016/j.apmt.2019.100496.
554 [8] L. Chen, Q. Shi, Y. Sun, T. Nguyen, C. Lee, S. Soh, Controlling Surface Charge
555 Generated by Contact Electrification: Strategies and Applications, Adv Mater
556 30(2018) e1802405, https://doi.org/10.1002/adma.201802405.
557 [9] Y. Bai, L. Xu, S. Q. Lin, J. J. Luo, H. F. Qin, K. Han, Z. L. Wang, Charge
558 Pumping Strategy for Rotation and Sliding Type Triboelectric Nanogenerators,
559 Adv. Energy Mater. 10(2020) 2000605,
560 https://doi.org/10.1002/aenm.202000605.
561 [10] Y. L. Zi, C. S. Wu, W. B. Ding, Z. L. Wang, Maximized Effective Energy Output
562 of Contact-SeparationTriggered Triboelectric Nanogenerators as Limited by Air
563 Breakdown, Adv. Funct. Mater. 27(2017) 1700049,
564 https://doi.org/10.1002/adfm.201700049.
565 [11] L. Xie, L. Yin, Y. Liu, H. Liu, B. Lu, C. Zhao, T. A. Khattab, Z. Wen, X. Sun,
566 Interface Engineering for Efficient Raindrop Solar Cell, ACS Nano 16(2022)
567 5292-5302, https://doi.org/10.1021/acsnano.1c10211.
568 [12] X. Chen, Y. Liu, Y. Sun, T. Zhao, C. Zhao, T. A. Khattab, E. G. Lim, X. Sun, Z.
569 Wen, Electron trapping & blocking effect enabled by MXene/TiO2 intermediate
570 layer for charge regulation of triboelectric nanogenerators, Nano Energy
571 98(2022) 107236, https://doi.org/10.1016/j.nanoen.2022.107236.
572 [13] Y. Li, W. Zheng, H. Zhang, H. Wang, H. Cai, Y. Zhang, Z. Yang, Electron
573 transfer mechanism of graphene/Cu heterostructure for improving the stability
574 of triboelectric nanogenerators, Nano Energy 70(2020) 104540,
575 https://doi.org/10.1016/j.nanoen.2020.104540.
576 [14] Y. Park, Y. E. Shin, J. Park, Y. Lee, M. P. Kim, Y. R. Kim, S. Na, S. K. Ghosh,
577 H. Ko, Ferroelectric Multilayer Nanocomposites with Polarization and Stress
578 Concentration Structures for Enhanced Triboelectric Performances, ACS Nano
579 14(2020) 7101-7110, https://doi.org/10.1021/acsnano.0c01865.

[15] D. W. Kim, J. H. Lee, I. You, J. K. Kim, U. Jeong, Adding a stretchable deep-trap interlayer for high-performance stretchable triboelectric nanogenerators, Nano Energy 50(2018) 192-200, https://doi.org/10.1016/j.nanoen.2018.05.041.

[16] H. J. Hwang, D. Choi, The coupled effects of an electron blocking layer beneath tribomaterials for boosted triboelectric nanogenerators, Functional Composites and Structures 3(2021) 025004, https://doi.org/10.1088/2631-6331/abf850.

[17] X. Xie, X. Chen, C. Zhao, Y. Liu, X. Sun, C. Zhao, Z. Wen, Intermediate layer for enhanced triboelectric nanogenerator, Nano Energy 79(2021) 105439, https://doi.org/10.1016/j.nanoen.2020.105439.

[18] L. Zhou, D. Liu, Z. Zhao, S. Li, Y. Liu, L. Liu, Y. Gao, Z. L. Wang, J. Wang, Simultaneously Enhancing Power Density and Durability of Sliding-Mode Triboelectric Nanogenerator via Interface Liquid Lubrication, Adv. Energy Mater. 10(2020) 2002920, https://doi.org/10.1002/aenm.202002920.

[19] J. Kim, H. Ryu, J. H. Lee, U. Khan, S. S. Kwak, H. J. Yoon, S. W. Kim, High Permittivity CaCu3Ti4O12 Particle-Induced Internal Polarization Amplification for High Performance Triboelectric Nanogenerators, Adv. Energy Mater. 10(2020) 1903524, https://doi.org/10.1002/aenm.201903524.

[20] H. Jiang, H. Lei, Z. Wen, J. Shi, D. Bao, C. Chen, J. Jiang, Q. Guan, X. Sun, S.-T. Lee, Charge-trapping-blocking layer for enhanced triboelectric nanogenerators, Nano Energy 75(2020) 105011, https://doi.org/10.1016/j.nanoen.2020.105011.

[21] H.-W. Park, N. D. Huynh, W. Kim, C. Lee, Y. Nam, S. Lee, K.-B. Chung, D. Choi, Electron blocking layer-based interfacial design for highly-enhanced triboelectric nanogenerators, Nano Energy 50(2018) 9-15, https://doi.org/10.1016/j.nanoen.2018.05.024.

[22] G. Liu, A. Liu, F. Shan, Y. Meng, B. Shin, E. Fortunato, R. Martins, High-performance fully amorphous bilayer metal-oxide thin film transistors using ultra-thin solution-processed ZrO_x dielectric, Appl. Phys. Lett. 105(2014)

113509, https://doi.org/10.1063/1.4895782.

[23] G. Adamopoulos, S. Thomas, P. H. Wöbkenberg, D. D. C. Bradley, M. A. McLachlan, T. D. Anthopoulos, High-Mobility Low-Voltage ZnO and Li-Doped ZnO Transistors Based on ZrO2 High-k Dielectric Grown by Spray Pyrolysis in Ambient Air, Adv. Mater. 23(2011) 1894-1898, https://doi.org/10.1002/adma.201003935.

[24] Y. Wu, M. Yang, A. Chin, W. Chen, C. Kwei, Electrical Characteristics of High Quality La_2O_3 Gate Dielectric with Equivalent Oxide Thickness of 5 Å, IEEE Electron Device Lett. 21(2000) 341-343, https://ieeexplore.ieee.org/document/847374.

[25] J. Zhuang, Q.-J. Sun, Y. Zhou, S.-T. Han, L. Zhou, Y. Yan, H. Peng, S. Venkatesh, W. Wu, R. K. Li, Solution-Processed Rare-earth Oxide Thin Films for Alternative Gate Dielectric Application, ACS Appl. Mater. Interfaces 8(2016) 31128-31135, https://doi.org/10.1021/acsami.6b09670.

[26] A. De Asha, J. Critchley, R. Nix, Molecular adsorption characteristics of lanthanum oxide surfaces: the interaction of water with oxide overlayers grown on Cu (111), Surf Sci 405(1998) 201-214, https://doi.org/10.1016/S0039-6028(98)00044-2.

[27] T. Gougousi, D. Niu, R. W. Ashcraft, G. N. Parsons, Carbonate formation during post-deposition ambient exposure of high-*k* dielectrics, Appl. Phys. Lett. 83(2003) 3543-3545, https://doi.org/10.1063/1.1623316.

[28] Y. Zhao, M. Toyama, K. Kita, K. Kyuno, A. Toriumi, Moisture-absorption-induced permittivity deterioration and surface roughness enhancement of lanthanum oxide films on silicon, Appl. Phys. Lett. 88(2006) 072904, https://doi.org/10.1063/1.2174840.

[29] J. Kim, S. Choi, J.-W. Jo, S. K. Park, Y.-H. Kim, Solution-Processed Lanthanum-Doped Al_2O_3 Gate Dielectrics for High-mobility Metal-Oxide Thin-Film Transistors, Thin Solid Films 660(2018) 814-818,

https://doi.org/10.1016/j.tsf.2018.03.041.

[30] B. Yang, G. He, L. Zhu, C. Zhang, Y. Zhang, Y. Xia, F. Alam, Z. Sun, Low-Voltage-Operating Transistors and Logic Circuits Based on A Water-driven $ZrGdO_x$ Dielectric with Low-cost ZnSnO, ACS Appl. Electron. Mater. 1(2019) 625-636, https://doi.org/10.1021/acsaelm.9b00110.

[31] Y. Fang, C. Zhao, I. Z. Mitrovic, C. Zhao, High-Performance and Radiation-Hardened Solution-Processed ZrLaO Gate Dielectrics for Large-Area Applications, ACS Appl Mater Interfaces 13(2021) 50101-50110, https://doi.org/10.1021/acsami.1c13633.

[32] S.-H. Lee, T. Kim, J. Lee, C. Avis, J. Jang, Solution-processed gadolinium doped indium-oxide thin-film transistors with oxide passivation, Appl. Phys. Lett. 110(2017) 122102, https://doi.org/10.1063/1.4978932.

[33] Z. Lin, L. Lan, P. Xiao, S. Sun, Y. Li, W. Song, P. Gao, E. Song, P. Zhang, L. Wang, Effects of rare-earth element dopants in high-mobility InOx-based thin-film transistors, IEEE Electron Device Lett. 37(2016) 1139-1142, https://doi.org/10.1109/LED.2016.2593485.

[34] D. Liu, J. Robertson, Passivation of oxygen vacancy states and suppression of Fermi pinning in HfO2 by La addition, Appl. Phys. Lett. 94(2009) 042904, https://doi.org/10.1063/1.3076119.

[35] X. D. Huang, Y. Ma, J. Q. Song, P. T. Lai, High-Performance Amorphous InGaZnO Thin-Film Transistor with ZrLaO Gate Dielectric Fabricated at Room Temperature, J Disp Technol 12(2016) 1522-1527, https://doi.org/10.1109/jdt.2016.2630046.

[36] I. Babu, G. de With, Enhanced electromechanical properties of piezoelectric thin flexible films, Compos. Sci. Technol. 104(2014) 74-80, https://doi.org/10.1016/j.compscitech.2014.08.022.

[37] Z. Zheng, D. Yu, Y. Guo, Dielectric Modulated Glass Fiber Fabric-Based Single Electrode Triboelectric Nanogenerator for Efficient Biomechanical Energy

Harvesting, Adv. Funct. Mater. 31(2021) 2102431, https://doi.org/10.1002/adfm.202102431.

[38] M. P. Kim, C. W. Ahn, Y. Lee, K. Kim, J. Park, H. Ko, Interfacial polarization-induced high-k polymer dielectric film for high-performance triboelectric devices, Nano Energy 82(2021) 105697, https://doi.org/10.1016/j.nanoen.2020.105697.

[39] H. J. Hwang, H. Hong, B. G. Cho, H. K. Lee, J. S. Kim, U. J. Lee, W. Kim, H. Kim, K.-B. Chung, D. Choi, Band well structure with localized states for enhanced charge accumulation on Triboelectrification, Nano Energy 90(2021) 106647, https://doi.org/10.1016/j.nanoen.2021.106647.

[40] I. Firdous, M. Fahim, W. A. Daoud, Performance enhancement of triboelectric nanogenerator through hole and electron blocking layers-based interfacial design, Nano Energy 82(2021) 105694, https://doi.org/10.1016/j.nanoen.2020.105694.

[41] L. Jin, X. Xiao, W. Deng, A. Nashalian, D. He, V. Raveendran, C. Yan, H. Su, X. Chu, T. Yang, W. Li, W. Yang, J. Chen, Manipulating Relative Permittivity for High-Performance Wearable Triboelectric Nanogenerators, Nano Lett 20(2020) 6404-6411, https://doi.org/10.1021/acs.nanolett.0c01987.

[42] D. Park, S. Lee, C. V. Anh, P. Park, J. Nah, Role of a buried indium zinc oxide layer in the performance enhancement of triboelectric nanogenerators, Nano Energy 55(2019) 501-505, https://doi.org/10.1016/j.nanoen.2018.11.008.

[43] G. Z. Li, G. G. Wang, D. M. Ye, X. W. Zhang, Z. Q. Lin, H. L. Zhou, F. Li, B. L. Wang, J. C. Han, High-Performance Transparent and Flexible Triboelectric Nanogenerators Based on PDMS-PTFE Composite Films, Adv. Electron. Mater. 5(2019) 1800846, https://doi.org/10.1002/aelm.201800846.

[44] J. Chung, D. Heo, G. Shin, D. Choi, K. Choi, D. Kim, S. Lee, Ion-Enhanced Field Emission Triboelectric Nanogenerator, Adv. Energy Mater. 9(2019) 1901731, https://doi.org/10.1002/aenm.201901731.

[45] Z. Li, M. Zhu, Q. Qiu, J. Yu, B. Ding, Multilayered fiber-based triboelectric nanogenerator with high performance for biomechanical energy harvesting, Nano Energy 53(2018) 726-733, https://doi.org/10.1016/j.nanoen.2018.09.039.

[46] M. Lai, B. Du, H. Guo, Y. Xi, H. Yang, C. Hu, J. Wang, Z. L. Wang, Enhancing the Output Charge Density of TENG via Building Longitudinal Paths of Electrostatic Charges in the Contacting Layers, ACS Appl Mater Interfaces 10(2018) 2158-2165, https://doi.org/10.1021/acsami.7b15238.

[47] C. Wu, T. W. Kim, J. H. Park, H. An, J. Shao, X. Chen, Z. L. Wang, Enhanced Triboelectric Nanogenerators Based on MoS2 Monolayer Nanocomposites Acting as Electron-Acceptor Layers, ACS Nano 11(2017) 8356-8363, https://doi.org/10.1021/acsnano.7b03657.

[48] J. Wang, C. Wu, Y. Dai, Z. Zhao, A. Wang, T. Zhang, Z. L. Wang, Achieving ultrahigh triboelectric charge density for efficient energy harvesting, Nat Commun 8(2017) 88, https://doi.org/10.1038/s41467-017-00131-4.

[49] W. Seung, H.-J. Yoon, T. Y. Kim, H. Ryu, J. Kim, J.-H. Lee, J. H. Lee, S. Kim, Y. K. Park, Y. J. Park, S.-W. Kim, Boosting Power-Generating Performance of Triboelectric Nanogenerators via Artificial Control of Ferroelectric Polarization and Dielectric Properties, Adv. Energy Mater. 7(2017) 1600988, https://doi.org/10.1002/aenm.201600988.

[50] N. Cui, L. Gu, Y. Lei, J. Liu, Y. Qin, X. Ma, Y. Hao, Z. L. Wang, Dynamic Behavior of the Triboelectric Charges and Structural Optimization of the Friction Layer for a Triboelectric Nanogenerator, ACS Nano 10(2016) 6131-6138, https://doi.org/10.1021/acsnano.6b02076.

[51] J. Chen, H. Guo, X. He, G. Liu, Y. Xi, H. Shi, C. Hu, Enhancing Performance of Triboelectric Nanogenerator by Filling High Dielectric Nanoparticles into Sponge PDMS Film, ACS Appl Mater Interfaces 8(2016) 736-744, https://doi.org/10.1021/acsami.5b09907.

[52] B. Miao, R. Mahapatra, N. Wright, A. Horsfall, The role of carbon

contamination in voltage linearity and leakage current in high-k metal-insulator-metal capacitors, J. Appl. Phys. 104(2008) 054510, https://doi.org/10.1063/1.2973687.

[53] S. Gao, R. Wang, C. Ma, Z. Chen, Y. Wang, M. Wu, Z. Tang, N. Bao, D. Ding, W. Wu, F. Fan, W. Wu, Wearable high-dielectric-constant polymers with core-shell liquid metal inclusions for biomechanical energy harvesting and a self-powered user interface, J. Mater. Chem. A 7(2019) 7109-7117, https://doi.org/10.1039/c9ta01249d.

Figure Captions

Fig. 1 High-permittivity electron blocking layer (HPEBL) based triboelectric nanogenerator (TENG). (a) Schematic illustration of the interfacial LaZrO HPEBL based TENG (H-TENG). (b) Cross-sectional view scanning electron microscope (SEM) images of i) $La_{0.1}Zr_{0.9}O_x$ HPEBL with PDMS as the triboelectric layer and enlarged image, ii) unique $La_{0.1}Zr_{0.9}O_x$ layer, iii) ZrO_x layer and iv) $La_{0.2}Zr_{0.8}O_x$ layer. (c) Energy level diagram. (d) Concise recapitulation on relative permittivity and leakage current density at 1.5 MV/cm of ZrO_x, $La_{0.1}Zr_{0.9}O_x$, and $La_{0.2}Zr_{0.8}O_x$. (e) open-circuit voltage (V_{oc}), short-circuit current (I_{sc}) and transfer charge density (σ_{tr}) of different TENGs without LaZrO, with ZrO_x, $La_{0.1}Zr_{0.9}O_x$, and $La_{0.2}Zr_{0.8}O_x$, respectively. (f) V_{oc}, I_{sc} and σ_{tr} of TENGs with $La_{0.1}Zr_{0.9}O_x$ HPEBL with different thicknesses of 55 nm, 110 nm and 165 nm. (g) A summary of transfer charge density of TENGs with the intermediate layer [19-21, 37-52]. (h) *V*-*Q* curves of $La_{0.1}Zr_{0.9}O_x$ H-TENG under various external resistance load.

Fig. 2 Comparison between traditional TENG and $La_{0.1}Zr_{0.9}O_x$ H-TENG. (a) Working mechanism of electron blocking and enhanced polarization of the LaZrO intermediate layer within the TENG. (b) Potential simulation results of conventional TENG and $La_{0.1}Zr_{0.9}O_x$ H-TENG. (c) Surface potential distributions of i) pure PDMS before and ii) after contact electrification with an AFM tip, iii) PDMS with the interfacial $La_{0.1}Zr_{0.9}O_x$ HPEBL before and iv) after contact electrification with an AFM tip. (d) Concise contact potential difference and (e) surface potential decay with time of triboelectric PDMS layer without and with the interfacial $La_{0.1}Zr_{0.9}O_x$ HPEBL. (Insets show the surface roughness of PDMS). Energy band diagram of traditional TENG (f) before and (g) after contact electrification. Energy band diagram of $La_{0.1}Zr_{0.9}O_x$ H-TENG (h) before and (i) after contact electrification.

Fig. 3 Characterizations of the interfacial LaZrO HPEBL with a role of La doping concentrations varying from 0 to 20%. O 1s peaks and spectra deconvolution of (a) ZrO_x, (b) $La_{0.1}Zr_{0.9}O_x$, and (c) $La_{0.2}Zr_{0.8}O_x$. (d) Summarized calculated atomic percentages of M-O, $V_{o,}$ and M-OH. (e) The survey X-ray photoelectron spectroscopy (XPS) spectrum. (f) Thermogravimetric analysis-differential scanning calorimetry (TGA-DSC) results. The inset shows the X-ray diffraction (XRD) patterns.

Fig. 4 Metal-insulator-metal (MIM) device with Al/LaZrO/ITO structure. (a) Scheme illustration of the MIM device (Inset shows the optical photograph of the MIM device). (b) Areal capacitance-frequency (C_i-*f*), (c) leakage current density-electrical field (J_{leak}-E), and (d) Poole–Frenkel (PF) emission plot of $La_{0.1}Zr_{0.9}O_x$ and $La_{0.2}Zr_{0.8}O_x$ thin films. (e) Working mechanism of leakage current generation with different oxygen vacancies density.

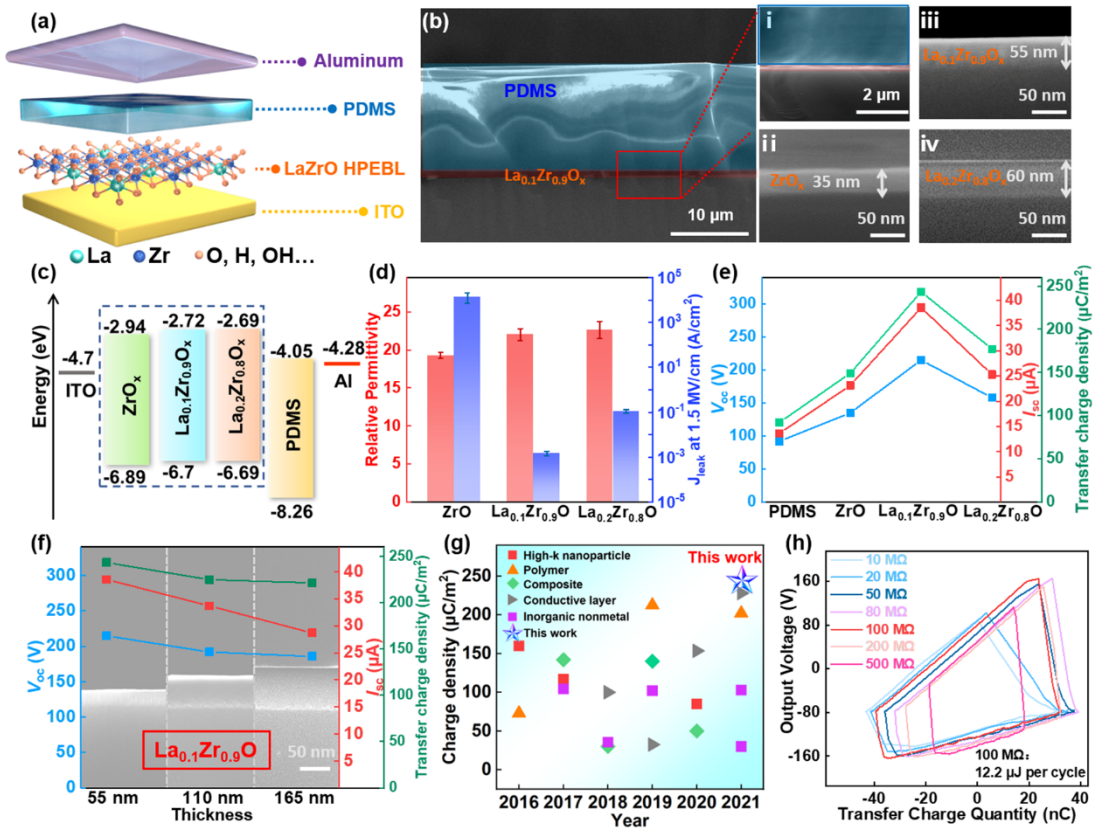
(a)
Aluminum
PDMS
LaZrO HPEBL
ITO
La
Zr
O, H, OH…
(b)
PDMS
$La_{0.1}Zr_{0.9}O_x$
10 μm
i
2 μm
ii
ZrO_x 35 nm
50 nm
iii
$La_{0.1}Zr_{0.9}O_x$ 55 nm
50 nm
iv
$La_{0.2}Zr_{0.8}O_x$ 60 nm
50 nm
(c)
Energy (eV)
-4.7
ITO
-2.94
-2.72
-2.69
ZrO_x
$La_{0.1}Zr_{0.9}O_x$
$La_{0.2}Zr_{0.8}O_x$
-6.89
-6.7
-6.69
-4.05
PDMS
-8.26
-4.28
Al
(d)
Relative Permittivity
J_{leak} at 1.5 MV/cm (A/cm²)
ZrO
$La_{0.1}Zr_{0.9}O$
$La_{0.2}Zr_{0.8}O$
(e)
V_{oc} (V)
I_{sc} (μA)
Transfer charge density (μC/m²)
PDMS
ZrO
$La_{0.1}Zr_{0.9}O$
$La_{0.2}Zr_{0.8}O$
(f)
V_{oc} (V)
I_{sc} (μA)
Transfer charge density (μC/m²)
$La_{0.1}Zr_{0.9}O$
50 nm
55 nm
110 nm
165 nm
Thickness
(g)
High-k nanoparticle
Polymer
Composite
Conductive layer
Inorganic nonmetal
This work
This work
Charge density (μC/m²)
2016 2017 2018 2019 2020 2021
Year
(h)
10 MΩ
20 MΩ
50 MΩ
80 MΩ
100 MΩ
200 MΩ
500 MΩ
Output Voltage (V)
100 MΩ:
12.2 μJ per cycle
Transfer Charge Quantity (nC)

Fig. 1

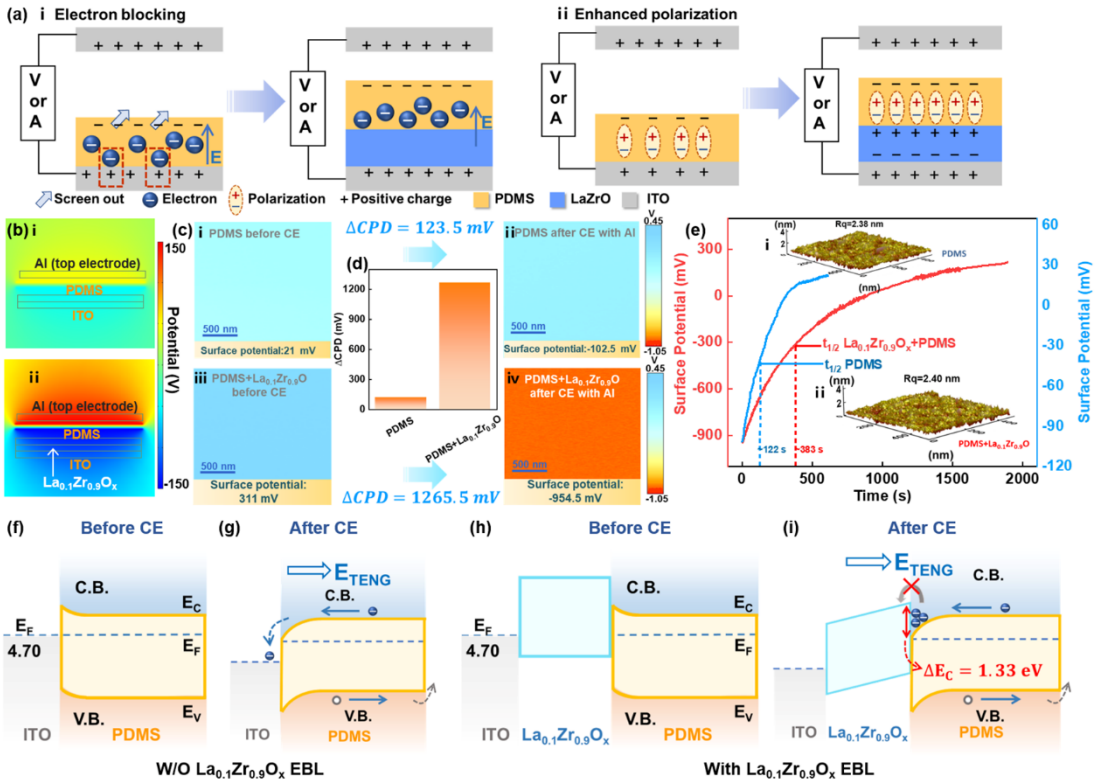
(a) i Electron blocking
ii Enhanced polarization
V or A
E
Screen out
Electron
Polarization
+ Positive charge
PDMS
LaZrO
ITO
(b) i
Al (top electrode)
PDMS
ITO
ii
Al (top electrode)
PDMS
ITO
$La_{0.1}Zr_{0.9}O_x$
(c) i PDMS before CE
500 nm
Surface potential:21 mV
iii PDMS+$La_{0.1}Zr_{0.9}O$ before CE
500 nm
Surface potential: 311 mV
Potential (V)
150
-150
$\Delta CPD = 123.5\ mV$
(d)
ΔCPD (mV)
1200
900
600
300
0
PDMS
PDMS+$La_{0.1}Zr_{0.9}O$
$\Delta CPD = 1265.5\ mV$
ii PDMS after CE with Al
500 nm
Surface potential:-102.5 mV
iv PDMS+$La_{0.1}Zr_{0.9}O$ after CE with Al
500 nm
Surface potential: -954.5 mV
V
0.45
-1.05
(e)
Surface Potential (mV)
300
0
-300
-600
-900
Time (s)
0
500
1000
1500
2000
60
30
0
-30
-60
-90
-120
Surface Potential (mV)
Rq=2.38 nm
PDMS
$t_{1/2}$ $La_{0.1}Zr_{0.9}O_x$+PDMS
$t_{1/2}$ PDMS
Rq=2.40 nm
122 s
383 s
PDMS+$La_{0.1}Zr_{0.9}O$
(f) Before CE
(g) After CE
(h) Before CE
(i) After CE
C.B.
E_C
E_F
E_V
E_F
4.70
V.B.
ITO
PDMS
E_{TENG}
$La_{0.1}Zr_{0.9}O_x$
$\Delta E_C = 1.33$ eV
W/O $La_{0.1}Zr_{0.9}O_x$ EBL
With $La_{0.1}Zr_{0.9}O_x$ EBL

Fig. 2

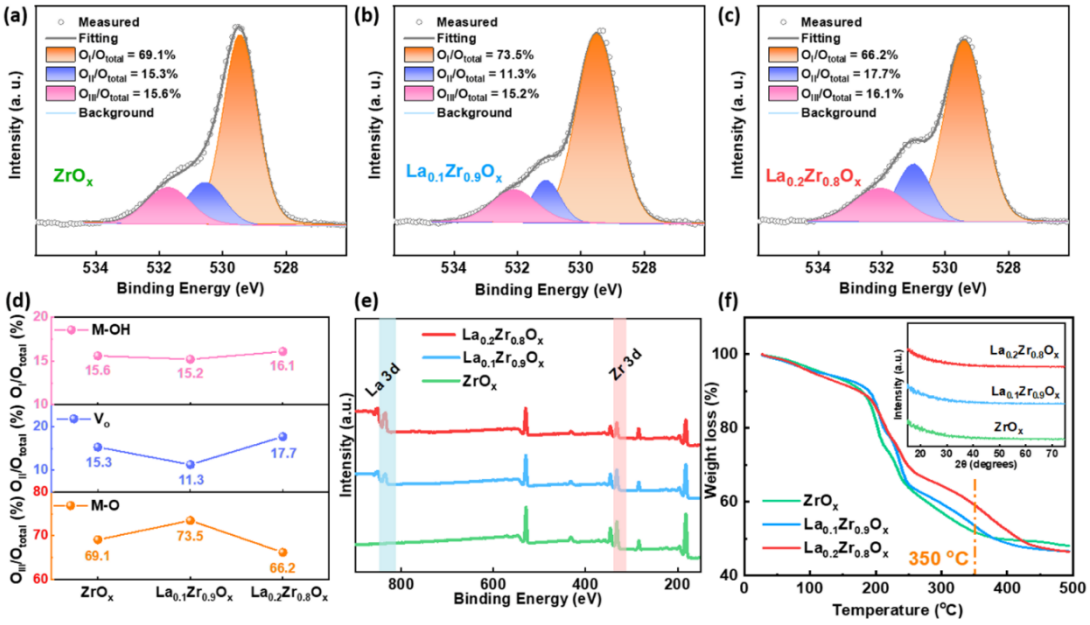

769

770 **Fig. 3**

771

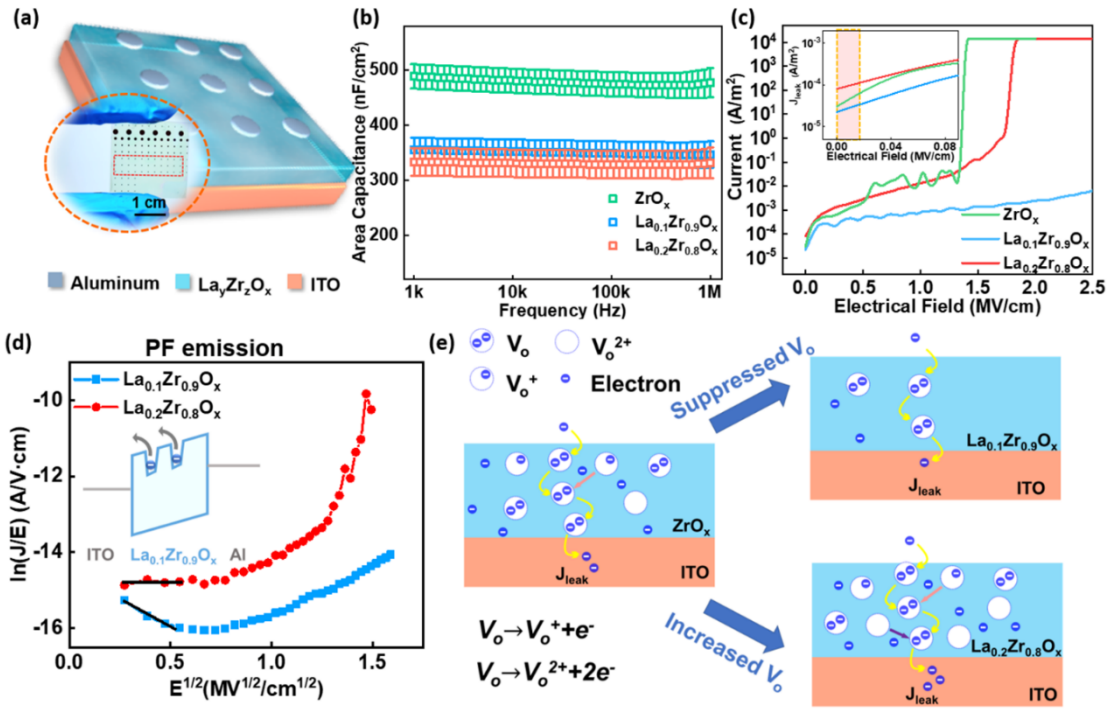

772

773 **Fig. 4**

774